

Positron annihilation lifetime spectroscopy of adipose, hepatic, and muscle tissues

Ashish V. Avachat

University of Illinois Urbana-Champaign

Anthony G Leja

University of Illinois Urbana-Champaign

Kholod H. Mahmoud

University of Illinois Urbana-Champaign

Mark A. Anastasio

University of Illinois Urbana-Champaign

Mayandi Sivaguru

University of Illinois Urbana-Champaign

Angela Di Fulvio (✉ difulvio@illinois.edu)

University of Illinois Urbana-Champaign

Article

Keywords:

Posted Date: May 25th, 2022

DOI: <https://doi.org/10.21203/rs.3.rs-1657111/v1>

License:  This work is licensed under a Creative Commons Attribution 4.0 International License.

[Read Full License](#)

Positron annihilation lifetime spectroscopy of adipose, hepatic, and muscle tissues

Ashish V. Avachat^a, Anthony G. Leja^b, Kholod H. Mahmoud^b, Mark A. Anastasio^a, Mayandi Sivaguru^c, and Angela Di Fulvio^{*b}

^aDepartment of Bioengineering, University of Illinois Urbana-Champaign

^bDepartment of Nuclear, Plasma, and Radiological Engineering, University of Illinois Urbana-Champaign

^cCytometry and Microscopy to Omics Facility, Roy J Carver Biotechnology Center, University of Illinois Urbana-Champaign

ABSTRACT

Can positron annihilation lifetime spectroscopy (PALS) be employed to discriminate different types of soft tissues? This work reports our experimental measurements of the three components of positron annihilation lifetime spectra for three types of bovine, non-fixated soft tissues: adipose, hepatic, and muscle. These three components of PALS spectra correspond to contributions from annihilation lifetimes of para-positronium (p-Ps), positron, and ortho-positronium (o-Ps). We also report a benchmark comparison between PALS and X-ray phase-contrast imaging, which is the current state-of-the-art for soft tissue imaging and analysis. Our measurements showed that the joint probability of annihilation from p-Ps and positron in the soft tissues increases with electron density of the tissue and hence correlates well with the mean voxel values measured by X-ray phase-contrast computed tomography. Notably, the o-Ps lifetime in adipose tissue (2.53 ± 0.01 ns) was approximately 25% longer than in hepatic (2.03 ± 0.02 ns) and muscle tissues (2.00 ± 0.01 ns). The significance here is that the o-Ps lifetime is a viable non-invasive probe for analyzing and discriminating the different soft tissues with a strong sensitivity to the lipid content of the tissue.

Introduction

Positron Annihilation Lifetime Spectroscopy (PALS) is a well-established, non-destructive analysis technique, widely used in the realm of material science since the seventies^{1,2}. PALS involves the use of positrons and their meta-stable products as probes for material characterization. In a material to be characterized, the positrons recombine with the electrons of the host material and annihilate by emitting two 511-keV photons that travel back-to-back. Before this annihilation, a positron can also interact with an electron by forming a bound exotic state called positronium (Ps). Such Ps can appear in two forms: para-positronium (p-Ps, with antiparallel spin) or ortho-positronium (o-Ps, with parallel spin). Typically, a p-Ps annihilates by emitting two 511-keV photons; and an o-Ps can either annihilate after recombining by emitting two 511-keV photons or decay by emitting three photons with a total energy of 1022 keV. Higher photon multiplicities are also allowed with a much lower probability³. The probability that o-Ps will annihilate after recombination (which results in 2γ emission) or will decay (which results in 3γ emission) depends on the host material properties—primarily, electron density and micro-structural void fraction. And, in materials with high electron density and low void fraction, the o-Ps is more likely to annihilate (2γ emission) than decay (3γ emission). This phenomenon results in a short mean lifetime of o-Ps in materials with high electron density and low void fraction. On the other hand, in materials with low electron density and high void fraction, the o-Ps can get trapped in the voids and is more likely to decay (3γ emission) than to annihilate (2γ emission). This interaction results in a longer mean lifetime of o-Ps than in materials with high electron density and a low void fraction. (Figure 1a illustrates the transport physics for a positron and prompt-gamma emitter ²²Na isotope.) For example, the mean lifetime of o-Ps in vacuum is approximately 140 ns⁴, but this lifetime can be as long as tens or hundreds of picoseconds in matter^{5,6}. The process of o-Ps annihilation after recombination with a lattice electron, which results in the 2γ emission, is also known as the o-Ps *pick-off*. A comprehensive review of Ps interactions with matter can be found in³.

Analytical representation of o-Ps interactions. Under a nonrelativistic approximation, the positron lifetime (λ) decreases with the electron density (N_e) of the medium: $\tau_{PS} = 1/\pi r_o^2 c N_e$, with $r_o = 2.8 \times 10^{-13}$ cm and c the speed of light². The measurement of o-Ps lifetime (τ_{o-Ps}) and the 3γ annihilation fraction ($f_{3\gamma}$)—i.e., the ratio of the 3γ annihilation events and the total number of annihilation events—can be used to characterize the density and size of defects and voids in the medium. Equation 1 applies to porous materials and shows that the o-Ps lifetime in the medium ($\tau_{o-Ps-medium}$) increases with the 3γ

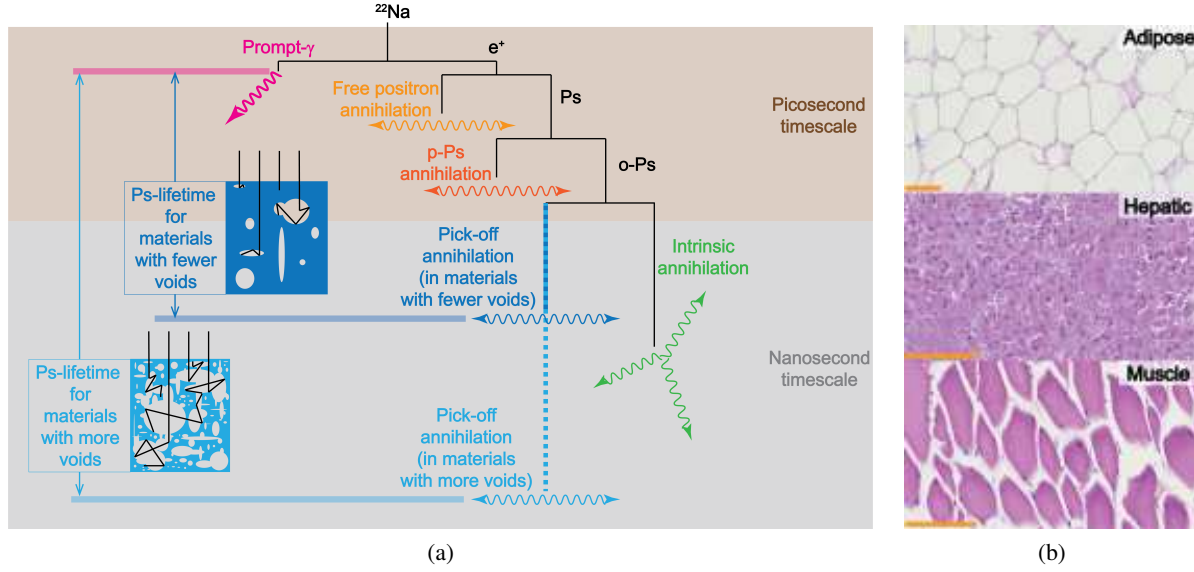


Figure 1. (a) Illustration for physics of positronium transport. ^{22}Na decays by emitting a prompt- γ and a positron, hereafter referred to as free positron (FP); FP can either directly annihilate by 2γ emission or can form positronium (Ps); Ps can form para-positronium (p-Ps) or ortho-positronium (o-Ps); p-Ps directly annihilates by 2γ emission; o-Ps can either annihilate by 2γ emission (pick-off annihilation) or intrinsically decay by 3γ emission; the pick-off annihilation depends on the void fraction for a given material, such that o-Ps annihilation by 2γ emission will occur earlier in a material with fewer voids than in a material with more voids. **(b) Histological photomicrographs of selected soft tissues.** Hematoxylin and eosin (H&E) stained histological photomicrographs for bovine adipose, hepatic, and muscle tissues. Scale bars represent $100\mu\text{m}$.

annihilation fraction⁷:

$$\tau_{o-Ps-medium} = \left(f_{3\gamma} - \frac{(-\frac{4}{3}P_{o-Ps})}{370} \right) \left(\frac{\tau_{o-Ps-vacuum}}{P_{o-Ps}} \right). \quad (1)$$

In Equation 1, P_{o-Ps} is the probability of o-Ps formation in the material, $\tau_{o-Ps-vacuum}$ is the o-Ps lifetime in vacuum, and the constant 370 is the computed ratio of cross sections of 2γ annihilation and 3γ annihilation ($\sigma_{2\gamma}/\sigma_{3\gamma} \approx 370$) for particles in free relative motion, as calculated by Ore and Powell using time-dependent perturbation theory⁴. The o-Ps lifetime is also directly related to the average void radius, R (Equation 2), as

$$\tau_{o-Ps-medium} = \frac{1}{\lambda_b} \left(1 - \frac{R}{R-\Delta} + \frac{1}{2\pi} \sin \left(\frac{2\pi R}{R+\Delta} \right) \right)^{-1}. \quad (2)$$

In Equation 2, λ_b is the spin-averaged positronium annihilation rate ($\lambda_b \approx 1/4\lambda_S = 2 \text{ ns}^{-1}$), and Δ is an experimentally measured parameter described by Goworek⁸. This theory shows that the positron lifetime directly decreases with an increase in electron density, but o-Ps lifetime ($\tau_{o-Ps-medium}$) increases with an increase in the average void size in the medium (Equation 2). Importantly, $\tau_{o-Ps-medium}$ and hence the average void size can be estimated by measuring the fraction of 3γ -decay events (Equation 1). The potential use of o-Ps lifetime to characterize biological tissues has been recently explored and the viability of using Ps and o-Ps lifetimes to analyze tissue properties, such as oxygen concentration and tissue porosity, has been reported⁹⁻¹¹. The presence of voids and defects results in a higher probability for the o-Ps to be trapped inside them, which in turn results in longer o-Ps-lifetime and a higher $f_{3\gamma}$, than the void-absent conditions. The measurement of the o-Ps-lifetime thus provides an indication of the concentration and type of the voids and local electronic density. In the biology domain, $f_{3\gamma}$ also decreases with the density of free radicals, which have unpaired electrons that easily undergo pick-off⁹. Using these mechanisms, some promising results have been previously reported in terms of discriminating between healthy and tumor tissues^{10, 12-14}, but a generalized characterization framework for discriminating different types of soft tissues has not yet been reported.

In this paper, we report the measured Ps lifetimes in bovine, non-fixated soft tissue samples: adipose, hepatic, and muscle (see Figure 1b for histological photomicrographs of the selected soft tissues). These experimental measurements agreed with the previously discussed theoretical relationships. To establish PALS as a probe for soft tissue analysis and to benchmark the sensitivity of the PALS to the subtle changes in the soft tissues, we compared its performance with the X-ray phase-contrast computed tomography (XPC-CT), which is the current state-of-the-art in non-invasive soft tissue analysis¹⁵.

Experimental results and discussion

We measured the PALS spectra for three different types of bovine, non-fixated soft tissues: adipose, hepatic, and muscle. These spectra, the objects of our analysis, consisted of the distribution of the differences in detection times between the 1.27 MeV ^{22}Na prompt decay gamma ray and the positron products—annihilation and decay gamma rays.

Analysis of the positronium annihilation lifetime spectrum

We resolved three components of lifetimes from the PALS spectra (Figure 2a). Each of these components characterizes one specific process of the positron interactions¹⁶. From the fastest to the slowest, the first component corresponds to p-Ps decay (τ_1, I_1), the second to the annihilation of free positrons (τ_2, I_2), and the third to o-Ps decay (τ_3, I_3)¹⁶. The PALS spectrum, $f(t)$, can be modeled as a convolution of the exponential decay functions corresponding to each process and the detector time resolution function (Equation 3), as follows:

$$f(t) = \sum_{i=1}^3 \frac{I_i}{\tau_i} e^{-\frac{t}{\tau_i}} * \frac{e^{-\frac{t^2}{2\sigma^2}}}{\sqrt{2\pi\sigma^2}} = \sum_{i=1}^3 \frac{I_i}{2\tau_i} e^{\frac{\sigma^2 - 2\tau_i t}{2\tau_i^2}} \operatorname{erfc}\left(\frac{\sigma^2 - \tau_i t}{\sqrt{2}\sigma\tau_i}\right). \quad (3)$$

In Equation (3), τ_i and I_i are the lifetime and intensity of the i -th component, and σ represents the detector time resolution (198.3 ± 0.8 ps)¹⁶. (We have reported the optimization results for the time response of our PALS experimental setup in detail in the past¹⁶). The first two decay constants of the overall Ps-lifetime—the ones that correspond to the p-Ps decay (τ_1) and to the free-positron (FP) annihilation (τ_2)—are comparable in the three types of tissues (Figure 2b). The third component of the PALS spectrum, o-Ps lifetime (τ_3), showed a significant difference for the adipose tissue compared to that of hepatic and muscle tissues (Figure 2b; the mean o-Ps lifetime for the adipose, hepatic, and muscle tissues: 2.53 ± 0.01 ns, 2.03 ± 0.02 ns, and 2.00 ± 0.01 ns, respectively).

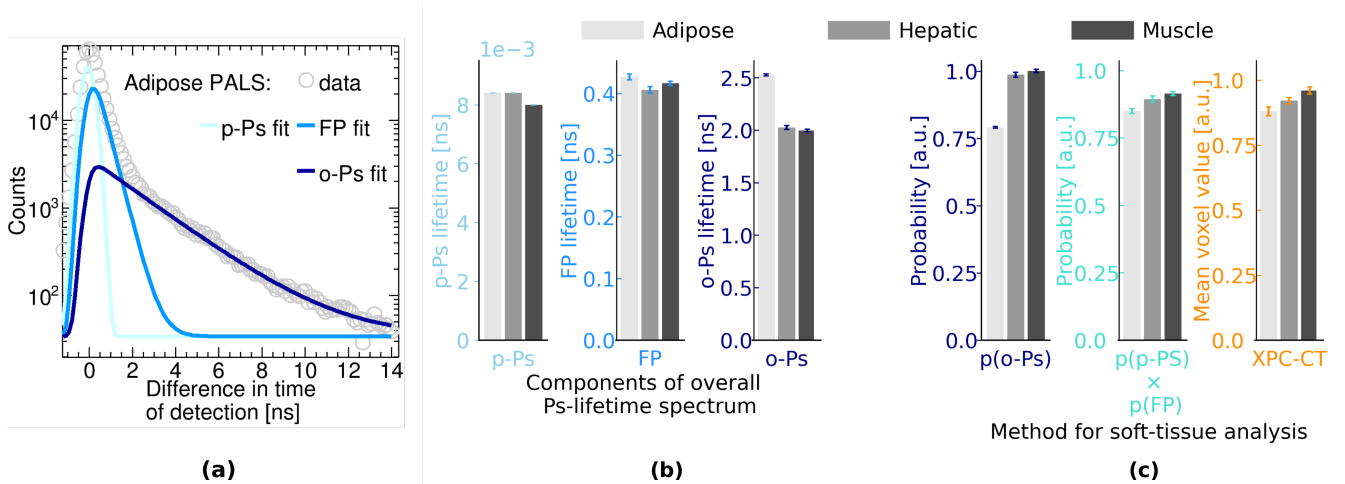


Figure 2. Results of PALS analysis and its benchmarking with XPC-CT. (a) The three components Ps-lifetime—p-Ps, free-positron (FP), and o-Ps lifetimes—can be decomposed from the measured PALS spectrum (example PALS spectrum and its decomposed components for adipose tissues in a). (b) The comparison of three components of the PALS spectrum for the three soft tissue samples showed that o-Ps is the most sensitive out of the three components for discerning the subtle changes between the different types of soft-tissue. (c) Comparison of measures based on PALS analysis method—probabilities of o-Ps annihilation ($p(o-Ps)$) and of p-Ps and free-positron annihilation ($p(p-Ps) \times p(FP)$)—and on XPC-CT.

PALS analysis for soft-tissue discrimination and its benchmarking with the current state-of-the-art

We found that the adipose tissue can easily be discriminated from the other two tissues by thresholding the o-Ps lifetime (or the probability of o-Ps annihilation, $p(o-Ps)$, i.e., the reciprocal of the o-Ps lifetime; Figure 2b and c). The difference between the $p(o-Ps)$ for hepatic and muscle tissues is subtle, yet discernible (Figure 2c). Interestingly, the joint probability of p-Ps and FP annihilation ($p(p-Ps) \times p(FP)$) can also enable us to discriminate the selected soft-tissue samples from each other. This joint $p(p-Ps) \times p(FP)$ increased from adipose to hepatic to muscle tissue (Figure 2c). Based on the previously discussed o-Ps transport physics, the significant differences in $p(o-Ps)$ for the selected tissues can be attributed to the differences in not only the electron densities and but also the void fractions for the selected tissues.

In order to experimentally corroborate these correlations of the $p(o-Ps)$ with the electron densities and void fraction and of the $p(p-Ps) \times p(FP)$ with electron density, we compared our o-Ps lifetime measurements with the current state-of-the-art in soft tissue analysis: X-ray phase-contrast based computed tomography (XPC-CT). The analysis of 3D image data from XPC-CT informed us about the relative contrast that is currently achievable and can be used for discriminating the selected soft tissues. The benchmarking with XPC-CT showed that the joint probability of p-Ps and FP annihilation ($p(p-Ps) \times p(FP)$) followed the same trend as the average voxel value for the selected soft-tissues (Figure 2b). The average XPC-CT voxel values for soft tissue samples depend on their electron densities, hence $p(p-Ps) \times p(FP)$ is directly proportional to the electron density of the soft tissues, as expected, theoretically. Similarly, we inferred that the electron density of the soft tissue affected the probability of o-Ps annihilation ($p(o-Ps)$), as theoretically expected (Equations 1 and 2). But, in addition, the microstructural void fraction affected the $p(o-Ps)$, which led to the significant difference between the $p(o-Ps)$ for adipose tissue and the other two soft-tissue types (Figure 2c). This effect of the void fraction was not captured by the XPC-CT because the sizes of microstructural voids were too small and, our XPC-CT system was insensitive to such microstructural voids.

Conclusion

We analyzed three types of bovine, non-fixated soft tissues—adipose, hepatic, and muscle—using positron annihilation lifetime spectroscopy (PALS). The PALS spectra included contributions from three annihilation lifetimes: p-Ps, free-positron, and o-Ps. We found that the joint probability of p-Ps and free-positron annihilation can be used to discriminate soft tissues. This combined probability showed a correlation to mean voxel values measured with low-energy X-ray phase-contrast CT imaging, confirming that the electron density drives the interaction probability of p-Ps and free-positron with matter. Conversely, we found that the o-Ps lifetime in adipose tissue is, on average, 25% longer than in hepatic and muscle tissues. Although it is known that o-Ps lifetime increases with porosity in inorganic materials; in biological tissue, o-Ps lifetime is the convolution of several phenomena, such as oxygen and free radical concentration, in addition to void fraction. The oxygen partial pressure was alike in all the measured samples, and no free radicals were induced in the tissues. Therefore, the significantly higher response of adipose tissue—in terms of o-Ps lifetime, when compared to hepatic and muscle tissue—can likely be ascribed to a higher void fraction, which was not resolved by the benchmarking XPC-CT imaging. The potential impact of this result in health sciences is that o-Ps annihilation lifetime can be used as a non-invasive probe for detecting and quantifying lipid content in soft tissues or organs.

Methods

We acquired consumer-grade bovine adipose, hepatic, and muscle tissue samples from a local butchery; no animals had to be sacrificed for this study. Each tissue sample was analyzed, consecutively, by PALS and XPC-CT in a non-fixated state, and then by histology after fixing.

PALS: measurements and analysis

We extracted the p-Ps, free positron (FP), and o-Ps lifetime components from the PALS spectra for bovine, non-fixated adipose, hepatic, and muscle tissues by using a ^{22}Na source and by recording the distribution of the differences in detection times between the 1.27 MeV ^{22}Na prompt decay gamma ray and the positron products—annihilation and decay gamma rays. In the experimental setup for PALS measurement (Figure 3a), a 1- μCi activity ^{22}Na source, the positron emitter, was placed between two samples of a given tissue type (one type at a time: adipose, hepatic, and muscle). By such sandwiching of the positron emitter with two samples, we maximized the tissue interaction and reduced the overall data acquisition time. This ^{22}Na source was encapsulated in thin Mylar foils, which ensured that most of the positrons emitted by the source reached the tissue samples. The ^{22}Na emits a positron, and the daughter nucleus de-excites in about 3 ps by emitting a 1.27 MeV gamma ray. Therefore, the emission of the 1.27 MeV was considered as a time stamp for the β^+ decay (positron emission time). During the irradiation, the approximate 1 cm \times 1 cm \times 1 cm tissue samples were kept at approximately 9 °C using a Peltier-based cooling system (Figure 3b). Two fast EJ-220 plastic organic scintillators of 5.08 cm length and 5.08 cm diameter coupled to 9214B ETEL photomultiplier vacuum tubes (PMT) were used to detect gamma rays in coincidence. We selected EJ-220 for this experiment because it exhibits a time resolution of 183 ± 0.8 ps¹⁶, hence being one of the fastest scintillation detectors commercially available. We used a high voltage power supply (DT5533EN, CAEN Technologies) to power the PMTs. The detected pulses were directly digitized by a 14-bit 500 MSps digitizer (DT5730, CAEN Technologies) and transferred to a workstation as full waveforms in binary format using the acquisition software CoMPASS¹⁷.

Each pulse, detected upon gamma-ray interaction in the scintillator, was associated with a time stamp. Accurate pulse timing is crucial to successfully reconstruct the PALS spectrum. Therefore, we developed and optimized a constant fraction discrimination (CFD) algorithm to accurately find each pulse onset time¹⁸. Digital CFD provides accurate timing and is superior to other timing algorithms (e.g., analog CFD or leading edge) in terms of time resolution when used for processing the organic

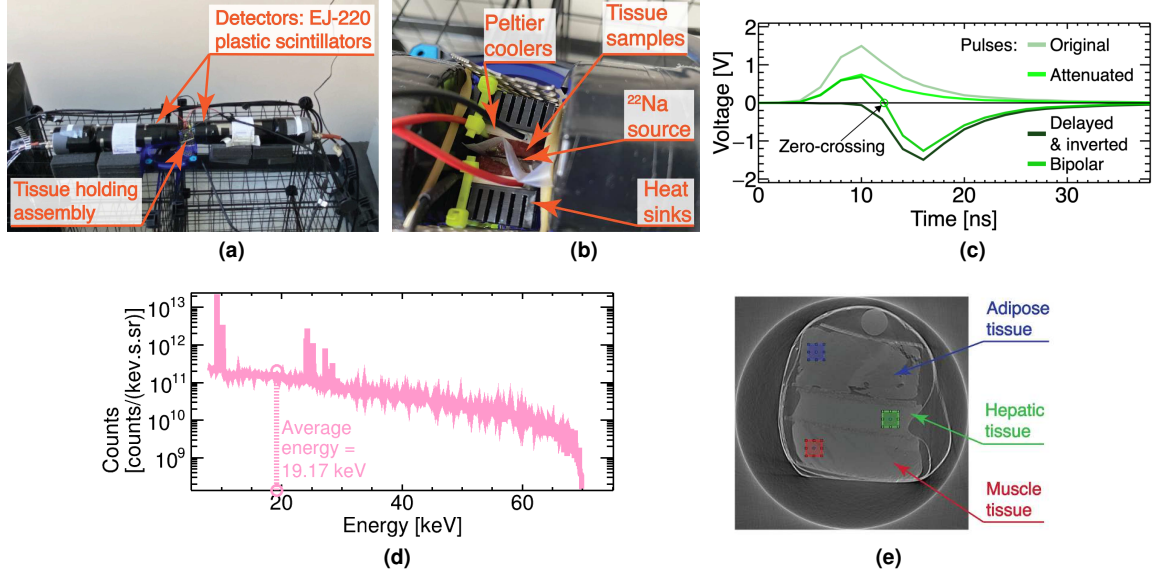


Figure 3. Methods for PALS analysis and its benchmarking with XPC-CT. (a) The PALS measurement setup: two scintillation detectors with a tissue sample in the middle irradiated by the ^{22}Na source. (b) ^{22}Na source placed between two tissue samples kept cooled by a Peltier-cell based system. (c) Sample fast pulse acquired by the organic scintillation detector, (1) its attenuated version by a factor F , (2) the original pulse delayed by Δ ns and inverted, and the (3) bipolar pulse obtained by subtracting (2) from the original pulse. The zero-crossing point corresponds to the pulse time stamp. (d) Energy spectrum and its average energy for 70 kVp X-ray beam from the liquid-metal-jet-based X-ray source used by XPC-CT system. (e) An example tomographic slice of XPC-CT images. The blue, green, and red boxes represent a 2D slice of the 3D regions-of-interest corresponding to the adipose, hepatic, and muscle tissues, respectively, in the given example XPC-CT slice.

scintillation pulses¹⁹. Pulses were digitized at a 500 MSps sampling frequency. We interpolated these digitized voltage values, one every 2 ns, to densely sample the rising edge, which typically lasts less than 10 ns. Each pulse can be modeled as the convolution between the sampled voltage values and a terminated *sinc* function (*tsinc*)²⁰. This model is detector-invariant and satisfies the Nyquist condition^{16,21}. The *tsinc* function is a *sinc* function modulated by a Gaussian function and is needed for time-finite, non-periodic signals. Equation 4 is the k -th linearly interpolated sample obtained after dividing the measurement sampling time into N intervals inside a window of width L , where $g_s(j)$ is the j -th sampling value of the input waveform:

$$G(j, k) = \sum_{i=0}^{L-1} g_s(j-i) \text{tsinc} \left(i + \frac{k}{N} \right) + g_s(j+1+i) \text{tsinc} \left(i + 1 - \frac{k}{N} \right). \quad (4)$$

After pulse interpolation, the time stamp was determined by the CFD algorithm:

$$\text{CFD}(l) = F \times g_s(l) - g_s(l - \Delta), \quad (5)$$

where $g_s(l)$ is l -th sample of interpolated pulse, with $l = j \times N + k$, $\text{CFD}(l)$ is a bipolar pulse with the zero-crossing point being the time stamp, the attenuation factor F (0-1) and time shift Δ are two data processing parameters that depend on the scintillator type. The pulse timing was obtained as the pulse zero-crossing time after subtracting the original pulse inverted and delayed by Δ nanoseconds from an attenuated version of the original pulse (Figure 3c). The optimum values for F and Δ are 0.4 ns and 4 ns, respectively¹⁶.

The annihilation and decay of the Ps in the tissue samples resulted in the emission of two or three gamma rays. The emission of two gamma rays in coincidence (the prompt 1.27 MeV followed by a lower energy gamma ray) was detected by the scintillator pair by applying a time gate of 200 ns, after determining the pulse detection times. The PALS spectra were created by histogramming the time interval between the arrival times of the 1.27 MeV decay gamma ray and of lower-energy annihilation or decay gamma rays. The inherent low energy resolution of organic scintillation detectors does not allow to discriminate 511 keV from lower energy gamma rays from 3γ decay, but their use in this study was mainly motivated by their fast response. As a result, the discrimination of the positron lifetime components was merely based on the cumulative PALS spectra. PALS spectra are well described by the linear combination of the three components: the fast decay of p-Ps, the slow

decay of free positron (FP), and the delayed decay of o-Ps (Equation 3). We used the software LT10²² to identify the three time constants. LT10's analysis provided the annihilation lifetimes and standard deviations of p-Ps, FP, and o-Ps in each tissue type. The error bars account for the propagation of the 1-standard-deviation uncertainties associated with the fitted parameters of lifetime distribution measured on multiple samples from the same tissue batch.

X-ray phase-contrast imaging: measurements and analysis

The X-ray phase-contrast imaging of the selected non-fixated soft tissues was performed using the propagation-based X-ray phase-contrast CT (XPC-CT) system of the Computational X-ray Imaging Science Laboratory at the Beckman Institute of the University of Illinois Urbana-Champaign. This XPC-CT system included: a liquid-metal-jet-based X-ray source (MetalJet D2, Excillum) operated at 70 kVp, 110 W power, and about 11 μm focal spot size; a CsI(Tl) scintillator-based X-ray imager with a pixel pitch of 13 μm and active area of about 54^2 mm^2 ($4\text{k} \times 4\text{k}$ X-Ray GSENSE SCMOS, Photonic Science); and an object manipulation system to rotate the imaging samples. A propagation distance (object-to-detector distance) of approximately 2 m was utilized to enhance the phase effects. This propagation distance, paired with the source-to-object distance of approximately 2 m, resulted in a magnification of 2 and Fresnel number of approximately 3.3 for an average X-ray energy of 19.17 keV for the 70 kVp X-ray energy spectrum of our liquid-metal-jet-based X-ray source (Figure 3d). A set of 700 projections was acquired to fully scan the imaging object (0° to 360°) with an exposure time of about 2.3 s per projection. Paganin's phase-retrieval toolbox, ANKAPhase, was used to recover the phase map for each projection²³. An in-house implementation of the Feldkamp, Davis, and Kress (FDK) algorithm was used to reconstruct the tomographic volume from the phase-contrast enhanced projections²⁴. For XPC-CT scanning, a PMMA rod and the three soft tissue samples were stacked together, with thin cardboard pieces separating them. This assembly was taped together tightly such that the field-of-view (FOV= 2.7 mm) had the following sequence (top to bottom in Figure 3e): PMMA rod, adipose sample, hepatic sample, and muscle sample. The average pixel values and standard deviations for each tissue type were calculated by randomly inserting 3D regions-of-interest (100^3 voxels) with ten repeats.

Histology: measurements and analysis

The selected soft tissue samples were fixed under pressure and vacuum with 10% formalin after PALS measurement and XPC-CT imaging. Then fixed samples were embedded in paraffin, and ten slices of 8-10 micron thickness were cut using a microtome from each block sample (1 cm^3). Two sections were extracted from each slice. Out of the ten slides for each type of sample, five were stained using Mason's Trichrome and the remaining five using hematoxylin and eosin. Microscopy was performed using a Hamamatsu Nanozoomer using a 20x 0.75 NA Olympus objective.

Data Availability

The datasets used and/or analysed during the current study available from the corresponding author on reasonable request.

References

1. Gidley, D. W., Peng, H. G. & Vallery, R. S. Positron annihilation as a method to characterize porous materials. *Annu. Rev. Mater. Res.* **36**, 49–79, DOI: [10.1146/annurev.matsci.36.11904.135144](https://doi.org/10.1146/annurev.matsci.36.11904.135144) (2006).
2. Tao, S. J. Positronium annihilation in molecular substances. *The J. Chem. Phys.* **56**, 5499–5510, DOI: [10.1063/1.1677067](https://doi.org/10.1063/1.1677067) (1972).
3. DeBenedetti, S. New atoms - positronium and mesonic atoms. *Il Nuovo Cimento* **4**, 1209–1270, DOI: [10.1007/BF02744346](https://doi.org/10.1007/BF02744346) (1956).
4. Ore, A. & Powell, J. L. Three-photon annihilation of an electron-positron pair (1949).
5. Van Horn, J. D., Wu, F., Corsiglia, G. & Jean, Y. C. Asymmetric positron interactions with chiral quartz crystals? In *Defect and Diffusion Forum*, vol. 373, 221–226, DOI: [10.4028/www.scientific.net/DDF.373.221](https://doi.org/10.4028/www.scientific.net/DDF.373.221) (Trans Tech Publ, 2016).
6. Gidley, D. *et al.* Positronium annihilation in mesoporous thin films. *Phys. Rev. B* **60**, R5157, DOI: [10.1103/PhysRevB.60.R5157](https://doi.org/10.1103/PhysRevB.60.R5157) (1999).
7. Jasiska, B. *et al.* Human tissue investigations using pals technique - free radicals influence. vol. 132, 1556–1558, DOI: [10.12693/APhysPolA.132.1556](https://doi.org/10.12693/APhysPolA.132.1556) (Polish Academy of Sciences, 2017).
8. Goworek, T. Positronium as a probe of small free volumes in crystals, polymers and porous media. *Annales UMCS, Chemia* **69**, 1–110, DOI: [10.2478/umcschem-2013-0012](https://doi.org/10.2478/umcschem-2013-0012) (2015).
9. Jasińska, B. *et al.* Human tissues investigation using pals technique. vol. 48, 1737–1747, DOI: [10.5506/APhysPolB.48.1737](https://doi.org/10.5506/APhysPolB.48.1737) (Jagellonian University, 2017).

10. Stepanov, S. V., Byakov, V. M. & Stepanov, P. S. Positronium in biosystems and medicine: A new approach to tumor diagnostics based on correlation between oxygenation of tissues and lifetime of the positronium atom. *Phys. Wave Phenom.* **29**, 174–179, DOI: [10.3103/S1541308X21020138](https://doi.org/10.3103/S1541308X21020138) (2021).
11. Shibuya, K., Saito, H., Nishikido, F., Takahashi, M. & Yamaya, T. Oxygen sensing ability of positronium atom for tumor hypoxia imaging. *Commun. Phys.* **3**, DOI: [10.1038/s42005-020-00440-z](https://doi.org/10.1038/s42005-020-00440-z) (2020).
12. Moskal, P., Jasińska, B., Stępień, E. & Bass, S. D. Positronium in medicine and biology. *Nat. Rev. Phys.* **1**, 527–529, DOI: [10.1038/s42254-019-0078-7](https://doi.org/10.1038/s42254-019-0078-7) (2019).
13. Zgardzińska, B. *et al.* Studies on healthy and neoplastic tissues using positron annihilation lifetime spectroscopy and focused histopathological imaging. *Sci. Reports* **10**, 1–10, DOI: [10.1038/s41598-020-68727-3](https://doi.org/10.1038/s41598-020-68727-3) (2020).
14. Moskal, P. *et al.* Positronium imaging with the novel multiphoton PET scanner. *Sci. Adv.* **7**, 1–10, DOI: [10.1126/sciadv.abh4394](https://doi.org/10.1126/sciadv.abh4394) (2021).
15. Romell, J. *Virtual histology by laboratory x-ray phase-contrast tomography*. Ph.D. thesis, KTH Royal Institute of Technology (2021).
16. Fang, M., Bartholomew, N. & Di Fulvio, A. Positron annihilation lifetime spectroscopy using fast scintillators and digital electronics. *Nucl. Instruments Methods Phys. Res. Sect. A: Accel. Spectrometers, Detect. Assoc. Equip.* **943**, 162507, DOI: <https://doi.org/10.1016/j.nima.2019.162507> (2019).
17. CAEN Technologies. Compass multiparametric daq software for physics applications. <https://www.caen.it/products/compass/> (2020).
18. Pals pulse processing program based on the root framework. <https://gitlab.engr.illinois.edu/nml/pals>. Accessed: 2022-02-10.
19. Steinberger, W., Ruch, M., Di Fulvio, A., Clarke, S. & Pozzi, S. Timing performance of organic scintillators coupled to silicon photomultipliers. *Nucl. Instruments Methods Phys. Res. Sect. A: Accel. Spectrometers, Detect. Assoc. Equip.* **922**, 185 – 192, DOI: [10.1016/j.nima.2018.11.099](https://doi.org/10.1016/j.nima.2018.11.099) (2019).
20. Warburton, W. K. & Hennig, W. New algorithms for improved digital pulse arrival timing with sub-gsps adcs. *IEEE Transactions on Nucl. Sci.* **64**, 2938–2950, DOI: [10.1109/TNS.2017.2766074](https://doi.org/10.1109/TNS.2017.2766074) (2017).
21. Shannon, C. E. Communication in the presence of noise. *Proc. IEEE* **86**, 447–457, DOI: [10.1109/JPROC.1998.659497](https://doi.org/10.1109/JPROC.1998.659497) (1998).
22. Kansy, J. & Giebel, D. Study of defect structure with new software for numerical analysis of pal spectra. vol. 265, DOI: [10.1088/1742-6596/265/1/012030](https://doi.org/10.1088/1742-6596/265/1/012030) (Institute of Physics Publishing, 2011).
23. Weitkamp, T., Haas, D., Wegrzynek, D. & Rack, A. ANKAphase: Software for single-distance phase retrieval from inline X-ray phase-contrast radiographs. *J. Synchrotron Radiat.* **18**, 617–629, DOI: [10.1107/S0909049511002895](https://doi.org/10.1107/S0909049511002895) (2011).
24. Feldkamp, L. A., Davis, L. C. & Kress, J. W. Practical cone-beam algorithm. *J. Opt. Soc. Am. A* **1**, 612–619, DOI: [10.1364/JOSAA.1.000612](https://doi.org/10.1364/JOSAA.1.000612) (1984). [1312.3977](https://doi.org/10.1364/JOSAA.1.000612).

Acknowledgements

This work was funded in-part by the Nuclear Regulatory Commission, United States award number 31310018K0002. We thank Ms. Karen Doty for preparing the tissue samples for the histology analysis and Mr. Ming Fang for his help to setup the PALS experiment and use the LT10 software.

Author contributions statement

A. Avachat and A. Di Fulvio conceived the experiment(s); A. Avachat, A. Leja, K. Mahmoud, M. Sivaguru and A. Di Fulvio conducted the experiment(s) and processed the data, A. Avachat, A. Leja, K. Mahmoud, and A. Di Fulvio wrote the manuscript; A. Avachat, and A. Di Fulvio analyzed the results. All authors reviewed the manuscript.